

# Non-metallic Cation Storage using Poly(3,4-ethylenedioxythiophene) Shells

Xin Rui Dou,<sup>[a]</sup> Qing Yu Meng,<sup>[a]</sup> and Hong Zhong Chi<sup>\*[a]</sup>

Previous studies propose that  $\text{NH}_4^+$  storage in metal oxides and metallic ion storage using Poly(3,4-ethylenedioxythiophene) (PEDOT) both undergo diffusion-controlled processes. This study, employing experimental and simulation studies, reveals that flower-like PEDOT shells predominantly store  $\text{NH}_4^+$  ions storage through surface-controlled processes, constituting over 80 percent of the overall storage.  $\text{NH}_4^+$  ions interact with PEDOT's  $\pi-\pi$  stacking via van der Waals interactions, circumventing ionization energy and entropy barriers. Additionally,

the controlled polymerization and crystallinity of PEDOT contribute significantly to this storage process. The reduction in lamellar packing distance and face-to-face distance between the molecular chains, coupled with an increase in crystalline domains, intensifies inter-chain weak interactions and extends the overlap length of wave functions. These findings offer a comprehensive insight into cation storage using organic polymers.

## 1. Introduction

Following the discovery of polyacetylene,<sup>[1]</sup> conducting polymers, like poly(thiophene), poly(pyrrole), poly(phenylenevinylene), poly(aniline), etc., have attracted widespread interest in both scientific research and practical applications. Among them, poly(3,4-ethylenedioxythiophene) (PEDOT) stands out as one of the most promising candidate for commercial applications in solar cells, electrochromic displays, thermoelectric devices, technical coatings, biosensors and supercapacitors due to its superior conductivity, biocompatibility, electrochromic activity, and chemical stability.<sup>[2-4]</sup> PEDOT is the polymerization product of monomer 3,4-ethylenedioxythiophene (EDOT). Three main synthetic routes are usually used: (i) electrochemical polymerization,<sup>[5]</sup> (ii) vapor phase polymerization<sup>[6]</sup> and (iii) chemically oxidative polymerization.<sup>[7]</sup> Electrochemical and vapor phase polymerization techniques are commonly used for thin film production. Slightly differently, PEDOT films with a special morphology can be produced through specially designed vapor-phase processes. For example, sheet-like PEDOT was obtained using an amphiphilic triblock copolymer in a vacuum vapor phase polymerization,<sup>[8]</sup> and freestanding nanofibrillar PEDOT films were synthesized via a reactive vapor-phase polymerization.<sup>[9]</sup> Oxidative chemical polymerization in solutions containing an oxidant such as ferric chloride or persulfates is the most common and classic method.<sup>[10]</sup> This technique offers versatility in producing PEDOT with various morphologies – free-standing nanowires were synthesized by using sodium dodecyl sulfate;<sup>[11]</sup> three-dimensional dendrites were hydrothermally deposited on carbon fiber cloth in an ethanol/water mixture solution;<sup>[12]</sup> and chains were prepared in the presence

of NaCl and formic acid.<sup>[13]</sup> The morphology and crystallinity of PEDOT directly determines its performance. For instance, 1D single-crystals nanowires has a conductivity as high as  $8797 \text{ Scm}^{-1}$ <sup>[14]</sup> whereas the highest data for a thin film is  $6259 \text{ Scm}^{-1}$ .<sup>[6]</sup> The reason is that conduction occurs in 2D or 3D<sup>[15]</sup> is inherently less efficient than 1D geometries.<sup>[16]</sup> Furthermore, unique morphologies can enhance the extent of reactive interfaces in contact with the electrolyte when used as electrochemically active materials, facilitating charge transfer during charging and discharging.

To date, the charge carriers used for electrochemical energy conversion and storage are mainly metal cations, i.e.,  $\text{Li}^+$ ,  $\text{Na}^+$ ,  $\text{K}^+$ ,  $\text{Ca}^{2+}$ ,  $\text{Mg}^{2+}$ ,  $\text{Zn}^{2+}$  as well as  $\text{Al}^{3+}$  ions, while reports on non-metallic cations, such as proton ( $\text{H}^+$ ), hydronium ion ( $\text{H}_3\text{O}^+$ ) and ammonium ion ( $\text{NH}_4^+$ ), are relatively few.<sup>[17-19]</sup> Compared with metallic ions, non-metallic exhibit advantages, including lighter molecular weight, smaller hydrated ionic size and more stable topochemistry. These properties make them interact with electrochemically active materials (insertion/de-insertion or ammoniation/de-ammoniation) with nearly zero strain<sup>[20-22]</sup> and align with the requirements of the next-generation aqueous batteries, addressing concerns of cost, safety, and performance for large-scale energy storage. Ji's group pioneered the use of  $\text{NH}_4^+$  and  $\text{H}^+$  as charging carriers in several aqueous batteries, achieving super-fast rate capability (up to 4000 C) and excellent cyclic stability (up to 0.73 million cycles).<sup>[23]</sup> This performance is nearly equivalent to that of an electrical double-layer capacitor. They attributed this pseudocapacitive-dominated behavior to the smaller non-metallic ionic size, enabling rapid transportation in the electrolytes and reducing the diffusion resistance in the electrode materials. Moreover, they proposed a monkey-swinging model based on hydrogen bonds chemistry to explicate the interaction between non-metallic ions and electrode active materials, rather than the ionic bonds between metallic cations and their electrode hosts. Recent work by Zhi and co-workers, utilizing hexagonal

[a] X. Rui Dou, Q. Yu Meng, H. Zhong Chi

College of Materials and Environmental Engineering, Hangzhou Dianzi University, Hangzhou 310018, People's Republic of China  
E-mail: hzchi@hdu.edu.cn

$\text{MoO}_3$  for  $\text{NH}_4^+$  storage, demonstrated non-diffusion-controlled pseudocapacitive behavior and reversible building-breaking interactions of hydrogen bonds during ammoniation/de-ammoniation.<sup>[24]</sup>

Naturally, organic materials, especially those with aromatic ring, are prone to interacting with non-metallic charge carriers through covalent bonds, hydrogen bonds or Van der Waals interactions that follow the donor-acceptor principle by delocalizing electrons between electrode materials and charge carriers.<sup>[25–28]</sup> PEDOT has been used in supercapacitor since the very beginning of its discovery, and its electrochemical performance is highly dependent upon its morphology and chemical/physical structure.<sup>[29–31]</sup> Inspired by these, we prepared flower-like PEDOT shells for aqueous  $\text{NH}_4^+$  storage. The relationships among preparation parameters, microstructure and charge storage mechanism were thoroughly investigated. We found that the PEDOT shells efficiently store charges through surface-controlled processes. Density functional theory analysis revealed enhanced  $\pi-\pi$  interactions between the progressively ordered macromolecules and the weak interactions between the  $\text{NH}_4^+$  and the PEDOTs. The exploration of hierarchical conducting polymer for aqueous non-metallic cations storage, coupled with a deeper understanding of the interactions between organic active materials and cations, will promote the development of next-generation energy storage devices towards safe, inexpensive and high power applications.

## Experimental

### Preparation of the PEDOT shells

3,4-ethylenedioxythiophene (EDOT), ferric chloride ( $\text{FeCl}_3$ ), methanol, sulfuric acid ( $\text{H}_2\text{SO}_4$ , 98%), and ammonium sulfate ( $(\text{NH}_4)_2\text{SO}_4$ ) were analytical and were not further purified.

To prepare the PEDOT shells, an amount of  $\text{FeCl}_3$  was added into 50 mL of boiling water and kept in a sealed container for one hour. The solution was cooled naturally. After centrifugation, the precipitate was collected. Then, 15  $\mu\text{L}$  EDOT was added into 10 mL methanol solution (20 Vol.% water + 80 Vol.% methanol) using a micropipette. The methanol solution was mixed with the precipitate under vigorous stirring and finally sealed and left to stand for 72 hours under ambient conditions. After sequential centrifugal washing with methanol and water to remove the residual reactants, the prepared product was rinsed several times with 0.1 M  $\text{H}_2\text{SO}_4$  to get rid of the iron oxyhydroxides or oxides. The final product was centrifugally washed with water, followed by freeze-drying. The concentrations of the  $\text{FeCl}_3$  solutions were 3.75, 7.5, 15, 30 and 60  $\text{g L}^{-1}$ , respectively, and accordingly, the as-prepared PEDOT shells were named as PEDOT-03, PEDOT-07, PEDOT-15, PEDOT-30 and PEDOT-60, respectively.

The preparation process for the PEDOT coatings on the iron oxides is the same except for the acid-cleaning.

The preparation process for the iron oxyhydroxides or oxides templates is the same except for the addition of EDOT monomers and the acid-cleaning.

## Characterizations

The microscopic morphology of the PEDOT shells was observed with a scanning electron microscope (SEM, Sirion-100, the Netherlands). Their crystallographic structure was characterized using small and wide angle X-ray scattering (SAXS/WAXS, Bruker, USA) and Fourier infrared spectroscopy (FT-IR, Shimadzu, Japan). After pressing into tablet, the electrical conductivity of the PEDOTs was measured with a four-point probe.

## Electrochemical Performance

The charge storage capability of the prepared PEDOTs was explored by means of cyclic voltammetry (CV) and galvanostatic charge/discharge (GCD) using an electrochemical workstation (IVium, the Netherlands). The cycling stability of the electrodes was tested through 5000 charge/discharge cycles at a scan rate of 100  $\text{mV s}^{-1}$ . All these measurements were done using a saturated calomel reference electrode and a platinum plate counter electrode in 0.5 M  $(\text{NH}_4)_2\text{SO}_4$  solution at approximately 25 °C. The working electrode was made by coating the PEDOTs on carbon paper (Toray, Japan), and the loading is about 2  $\text{mg cm}^{-2}$ . The specific capacitance of the PEDOTs was calculated according to the following equation:

$$C = \frac{1}{mv(V_c - V_a)} \int_{V_a}^{V_c} I_v dV \quad (1)$$

Or

$$C = \frac{I_g t}{m(V_c - V_a)} \quad (2)$$

where C means the specific capacitance ( $\text{F g}^{-1}$ ), m is the mass of the active materials (g), v is the scan rate ( $\text{V s}^{-1}$ ),  $(V_c - V_a)$  denotes the sweep potential range during discharge (V) and  $I_v$  and  $I_g$  is the voltammetric current or galvanostatic current (A).

## Simulation details

Weak interactions between the lamellar packing, between the macromolecule chains, and between the macromolecules and cations were analyzed using independent gradient model based on Hirshfeld partition (IGMH) method<sup>[32]</sup> in Multiwfn program package<sup>[33]</sup> and rendered by VMD<sup>[34]</sup> software. In the models used for the simulations, the lamellar packing distance and the face-to-face distance between the macromolecular chains were determined on the base of the SAXS/WAXS results, and all the dangling carbon bonds were saturated with hydrogen atoms. The geometry optimization for electronic structure analysis was performed at the  $\omega\text{B97XD}/6-311\text{G}^{**}$  basis set using Orca program.<sup>[35]</sup> The periodic characteristics of the interactions were investigated using CP2K program<sup>[36]</sup> at the PBE-D3(BJ)/6-311G<sup>\*\*</sup> basis set, and the models for the simulations contain 3×3×3 EDOT monomers.

## 2. Results

### 2.1. Characterization

Ferric chloride ( $\text{FeCl}_3$ ) was selected as the oxidant for this study. Intrinsically, ferric ions ( $\text{Fe}^{3+}$ ) are of high hydrolyzability,<sup>[37]</sup> resulting in the formation of iron

oxyhydroxides.<sup>[38]</sup> The morphology of the hydrolysis products is mainly influenced by factors including  $\text{Fe}^{3+}$  concentration, composition, temperature, pH as well as precipitation time.<sup>[38]</sup> Under the given conditions of our investigation – ambient temperature of about 25 °C, a nearly neutral aqueous solution and a duration of 3 days – the morphology of the hydrolysis products at various concentrations is shown in Figure S1. As can be seen, the precipitate obtained from a 3.75 g L<sup>-1</sup>  $\text{FeCl}_3$  aqueous solution (Figure S1a) consists of thin strips. With increasing the concentration, these strips tend to laterally aggregate and grow into flower like hierarchical structures (Figure S1m). These oxyhydroxides were subsequently utilized as the source of the oxidant and served as a self-sacrificing template for the synthesis of hierarchical PEDOTs.

Figure 1a–c representatively show the iron oxyhydroxides, the PEDOT coatings on the oxyhydroxides and the hierarchical PEDOTs, respectively, (Figure S1 shows the morphologies produced at various  $\text{FeCl}_3$  concentrations). The inset in Figure 1b clearly shows the oxyhydroxides and the PEDOT coatings. After acid washing, the oxyhydroxide template is

completely removed, indicated by the absence of the Fe element's  $\text{K}\alpha$  signal at approximately 6.5 keV in the energy dispersive spectrometer (EDS) spectrum (Figure 1d) and the noise signal in the elemental mapping of Fe element (Figure 1g). Notably, the oxidant concentration affects the thickness of the coatings. PEDOT prepared with lower concentrations appears relatively soft (Figure S1c), whereas those prepared with higher concentrations exhibit greater stiffness (Figures S1i, S1l and S1o). According to the morphology shown in Figure S1a, the thin iron oxyhydroxide strips may only barely provide  $\text{Fe}^{3+}$  ions for the polymerization reaction. Consequently, both the nucleation and growth of the PEDOT proceed slowly, resulting in the thin coating (Figure S1c), and vice versa.

The FT-IR spectrums of the PEDOTs are presented in Figure 2 and Figure S2. In comparison with the one without acid washing, a broad peak appears at 3472 cm<sup>-1</sup> and the peak at 613 cm<sup>-1</sup> disappears (Figure S2). The appearance of the peak at 3472 cm<sup>-1</sup> suggests that the PEDOT shells contain a certain amount of water of crystallization or hydration. The

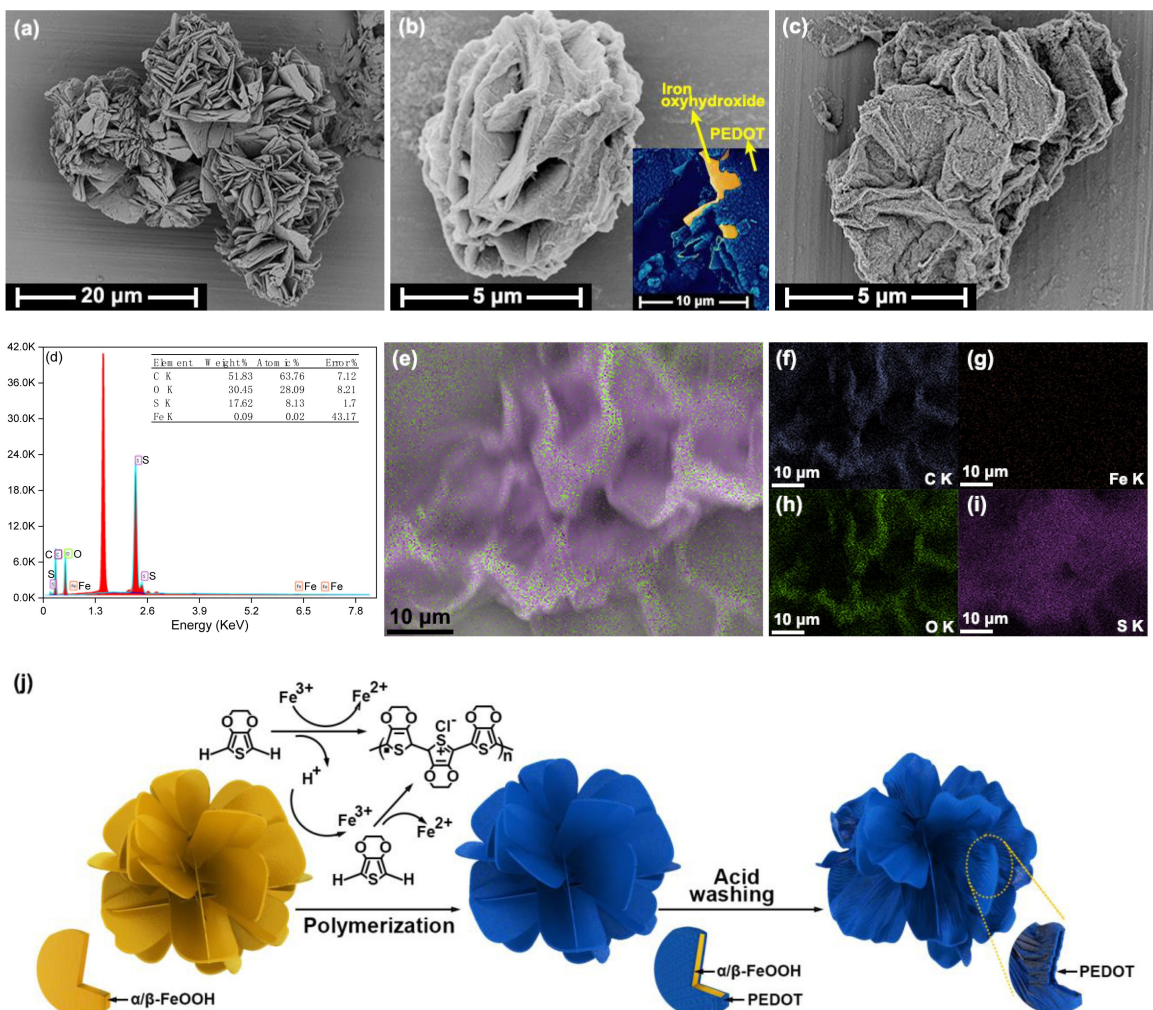


**Figure 1.** The SEM images of the iron oxyhydroxide (a), PEDOT coatings on the oxyhydroxide (b), and the PEDOT shells (c) produced with 30 g L<sup>-1</sup>  $\text{FeCl}_3$ ; The EDS spectrum (d) and the corresponding elemental mapping (e) of C (f), Fe (g), O (h), and S (i) of the PEDOT shells; A scheme for the formation of the PEDOT shells (j).

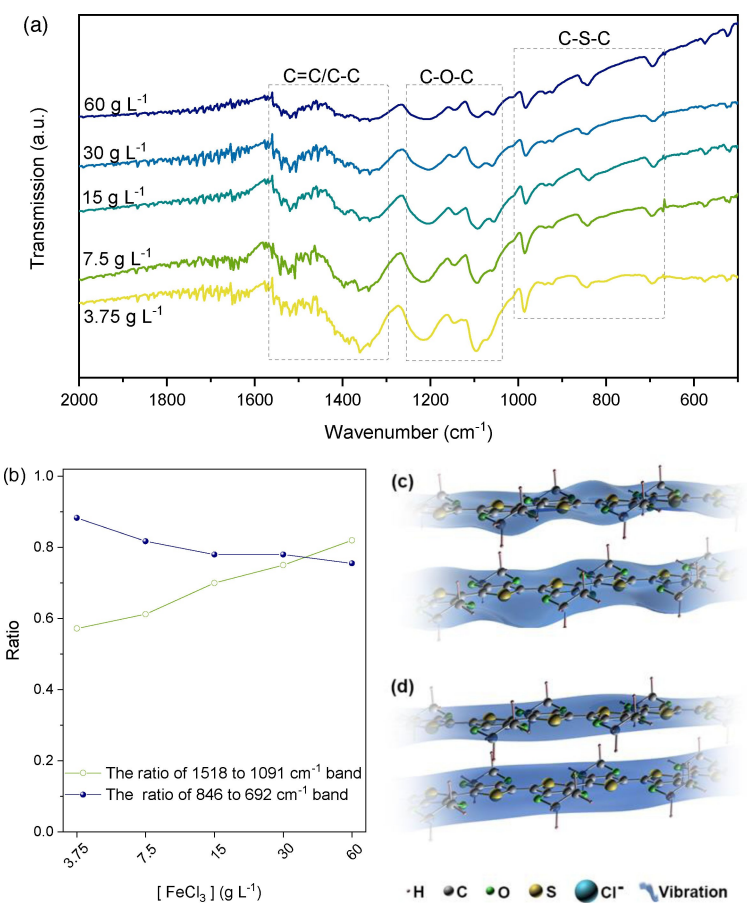


**Figure 2.** The FT-IR spectra of the PEDOT shells prepared with various concentrations of  $\text{FeCl}_3$  (a); The quinoid-to-ethylenedioxy ratio and the 846 to  $692 \text{ cm}^{-1}$  band integration ratio vs. the concentration of  $\text{FeCl}_3$  (b); Schematic diagram of the change in atomic dipole moment for the sample prepared with low (c) and high (d) concentration of  $\text{FeCl}_3$ .

peak at approximately  $613 \text{ cm}^{-1}$  is the typical absorption of iron oxyhydroxides according to the Mössbauer spectroscopic studies on the hydrolysis of iron(III) salt solutions.<sup>[39]</sup> Its disappearance aligns with the EDS results (Figure 1d and 1g). The other peaks at about 1518, 1358, 1209, 1149, 1091, 1056, 981 and 935  $\text{cm}^{-1}$  are the characteristic absorption of PEDOT. Specifically, the bands at 1518 and 1358  $\text{cm}^{-1}$  arise from the C=C asymmetric stretching and C-C inter-ring stretching of the quinoidal structure in the thiophene ring;<sup>[10]</sup> the bands at 1149 and 1056  $\text{cm}^{-1}$  originate from C–O–C stretching vibrations in the ethylenedioxy ring, and correspondingly, the bands at 1209 and 1091  $\text{cm}^{-1}$  are their bending vibration;<sup>[9]</sup> and the bands at 981 and 935  $\text{cm}^{-1}$ , along with those at 846 and 692  $\text{cm}^{-1}$ , stem from the C–S–C bond in the thiophene ring.<sup>[40]</sup>

The relative intensities of these bands can be used as indicators for inferring the degree of polymerization of the PEDOTs. In fact, determining the polymerization degree is challenging because PEDOT is insoluble. However, as shown in Figure 2a, the relative absorption intensities of the C=C/C–C bands and the C–O–C bands progressively weaken as the amount of the oxidant increases. It is well known that the range of variation of atomic dipole moments primarily

determines the intensity of an IR vibration absorption, so these gradually weakened intensities imply the suppression of the disordered mode of C=C/C–C bands in the thiophene ring and the arbitrarily stretching or bending vibrations of the C–O–C bands in the ethylenedioxy ring. In short, the groups in PEDOT macromolecules become progressively ordered. Quantitatively, the relative ratio between quinoid group ( $1518 \text{ cm}^{-1}$ ) and ethylenedioxy group ( $1091 \text{ cm}^{-1}$ ) can be regarded as a benchmark of conjugation length of the polymer, since the oxidative polymerization reforms benzoid to quinoid;<sup>[41]</sup> also, the integration ratio of the bands between 846 and  $692 \text{ cm}^{-1}$  can be used to evaluate the degree of the polymerization, higher ratios indicating lower polymerization.<sup>[7]</sup> We then calculated these ratios and depicted them in Figure 2b, in which both the upward trend of the quinoid-to-ethylenedioxy ratio and the downward trend of the 846  $\text{cm}^{-1}$  band to 692  $\text{cm}^{-1}$  band integration ratio support the improved polymerization with increasing  $\text{Fe}^{3+}$  ion concentration ( $\text{FeCl}_3$ ). The process is shown schematically in Figure 2c and 2d.

The arrangement and phase composition of the PEDOT shells were investigated using X-ray diffraction technique. The four diffraction peaks of orthorhombic PEDOT a distinguished

(Figure S3): the strong and sharp peak at  $6.3^\circ$  is associated with the Bragg diffraction of (100) plane; the peak at  $12.6^\circ$  is assigned to the (200) plane, which directly reflects the distance between two lamellar stacks;<sup>[7]</sup> the peak at  $17^\circ$  is challenging to index, but according to previous reports<sup>[13]</sup> and our FT-IR results, it could be the crystal water located near the polymer chains; and the broad peak at about  $25.9^\circ$  is ascribed to the diffraction of the (020) plane, which corresponds to the  $\pi-\pi$  stacking of the thiophene rings in the two-dimensional polymer packing. (The unacid-washed samples contain a complex phase composition including  $\alpha$ -FeOOH (74-2195),  $\beta$ -FeOOH (75-1594) and PEDOT, as illustrated in Figure S3.) The ordered growth of the macromolecules was further revealed through small and wide angle X-ray scattering (SAXS/WAXS).<sup>[29,42]</sup> The diffractograms are presented in Figure 3a, in which all observable peaks are sharper and larger for the

samples prepared at higher concentrations compared to those prepared at lower concentrations, implying that, consistent with the aforementioned FT-IR analysis, the ordering of the PEDOTs is ameliorated with the increasing amount of the oxidant.

Specifically, the peaks around  $q=0.78, 1.17$  and  $1.55 \text{ \AA}^{-1}$ , reflecting the periodicity of the embryonic macromolecules embodying a lot of distortion<sup>[42]</sup> are evident in the samples prepared at very low concentration, such as  $3.75$  and  $7.5 \text{ g L}^{-1}$ . However, they disappear in the PEDOTs prepared at higher concentrations, e. g.  $30$  and  $60 \text{ g L}^{-1}$ , indicating an improvement of crystallinity. The progressively shaped and stronger peak at  $q=0.45 \text{ \AA}^{-1}$  further unveil the gradually ordered lamellar packing. Correspondingly, the increasing trends of the peaks at  $q=0.9$  and  $1.8 \text{ \AA}^{-1}$  mean that the distance between the PEDOT lamellar packings [ $d(100)$ ] or the face-to-

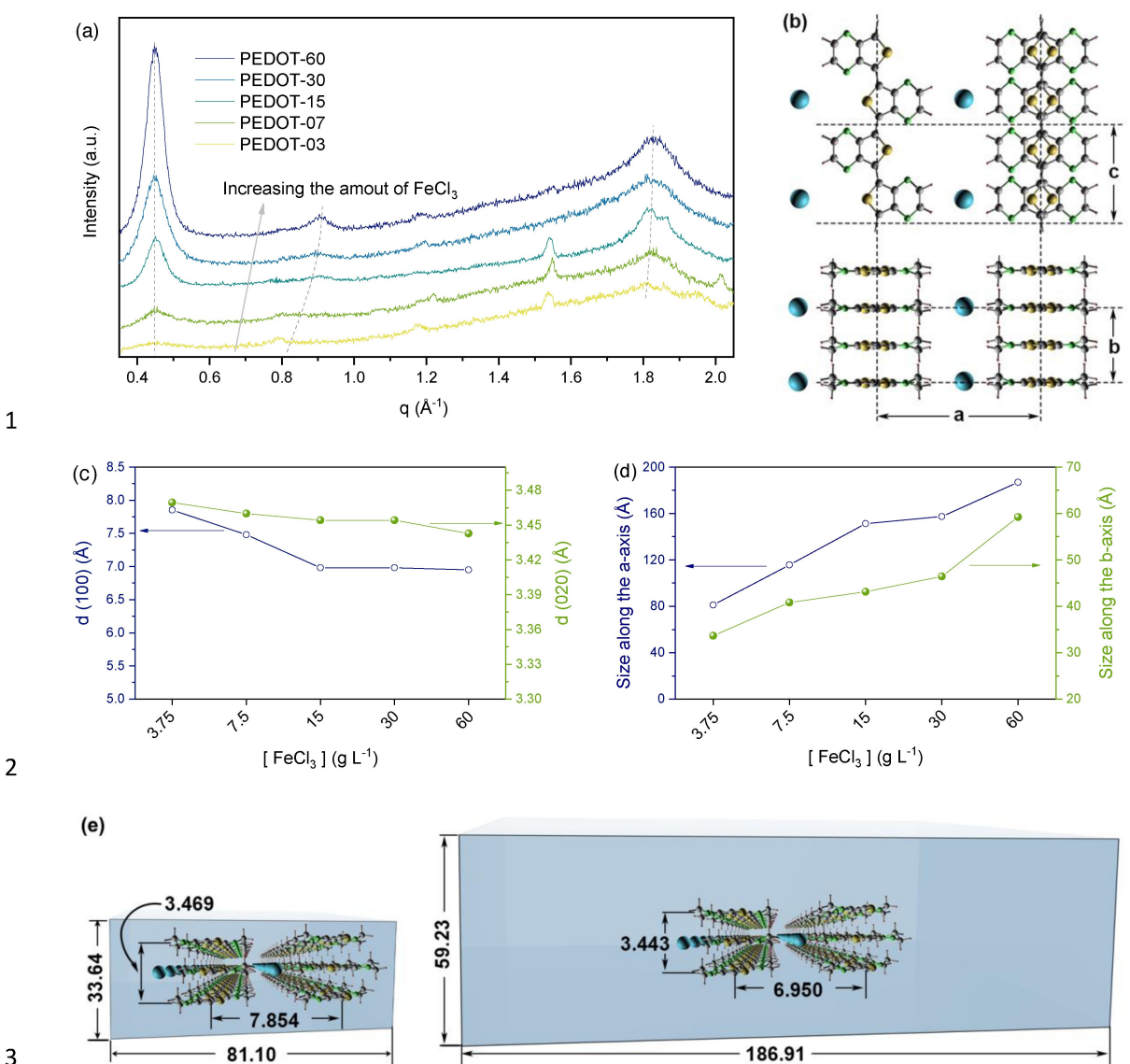


**Figure 3.** SAXS/WAXS profiles of the PEDOT shells prepared with various concentrations of  $\text{FeCl}_3$  (a); Illustration of the crystalline structure of PEDOT in projections along the b-axis (upper) and the c-axis (lower) direction (b); Variations in the distances between the PEDOT lamellar packing [ $d(100)$ ] and the face-to-face distance of PEDOT chains within an oligomer [ $d(020)$ ] (c); Variations in the grain sizes along the a-axis and b-axis (d); Schematic variations in interplanar spacing and grain size along the a-axis and b-axis for the sample prepared with  $3.75$  (left) and  $60 \text{ g L}^{-1}$  (right)  $\text{FeCl}_3$ , unit:  $\text{\AA}$  (e, f).

face distance of PEDOT chains [d(020)] within an oligomer becomes shorter (corresponding to the distances  $b$  and  $a$  in Figure 3b, respectively). These distances were then calculated: the d(100) shortened from 7.854 to 6.950 Å and the d(020) changed from 3.469 to 3.443 Å as the  $\text{FeCl}_3$  concentration increased from 3.75 to 60 g L<sup>-1</sup> (Figure 3c and 3e). The variations in crystallite size were also estimated according to Debye-Scherrer formula: for PEDOT-03, the size along the b-axis, derived from the (020) plane, is about 33.64 Å, and the size along the a-axis, derived from the (100) plane, is about 81.10 Å; while the dimensions become 59.23 and 186.91 Å for PEDOT-60, respectively (Figure 3d and 3e). These shortened distances (Figure 3c and Figure S4) lead to stronger interactions between the chains, which both inhibit arbitrarily stretching or bending vibrations of the chemical bands in the linear macromolecules and increase the degree of ordered alignment of the chains. In general, the higher the degree of ordering, the better the electrical conductivity.<sup>[43]</sup> The expanded microcrystallite domain (Figure 3d and Figure S4) apparently prolongs the electron mean-free path. Therefore, the PEDOTs shells should have excellent high-rate capability when used as electrochemically active materials.

## 2.2. Electrochemical performance

The charge storage performance of the PEDOTs was measured using  $\text{NH}_4^+$  ions as charge carriers. Figure 4a and 4b (also shown in Figure S5 and S6) illustrate their CV curves at various scan rates from 5 to 500 mV s<sup>-1</sup> and GCD curves at various current densities from 0.5 to 10 A g<sup>-1</sup>. Their rapid and stable responses upon switching the potentials demonstrate the

excellent reversibility of the charge storage processes on the PEDOTs. The resistance, as indicated by the ohmic drops in Figure 4b, is about 0.0162 mΩ. The nearly rectangular CV curves and the almost isosceles GCD curves are typical of capacitive characteristics of electric double-layers (EDL) materials.<sup>[44]</sup> It is well accepted that capacitive charge storage involves two fundamental mechanisms: the formation of EDL along electrode/electrolyte interfaces and highly reversible redox reactions occurring on or near electrode/electrolyte interfaces, known as pseudocapacitance.<sup>[44,45]</sup> The storage of  $\text{NH}_4^+$  by metal oxides falls into the latter case.<sup>[24]</sup> Conducting polymers, including PEDOT, also typically store charges through pseudocapacitive processes involving charge transfer, that is, PEDOT completes a charge storage process through counter ions move in and out.<sup>[12,46,47]</sup> This charge transfer process inevitably results in the rate performance of PEDOT being inferior to that of EDL materials. Nevertheless, the CV curves in Figure 3a remain a quasi-rectangular shape even at a high scan rate of 200 mV s<sup>-1</sup>, suggesting the excellent rate performance of our PEDOTs. Zozoulenko's group recently demonstrated that the capacitance of PEDOT: PSS (Poly(3,4-ethylenedioxothiophene):polystyrene sulfonate) arises from EDL by increasing the interfaces between nano-scaled PEDOT-rich and PSS-rich interconnected grains.<sup>[48]</sup> Likewise, the PEDOT shells may also store charges primarily through an EDL-like process.

To validate the charge storage mechanism of the PEDOTs, the analysis focused on their CV curves. When considering a current density ( $j$ , A g<sup>-1</sup>) at a specific voltage originating from surface-controlled and diffusion-controlled processes, the  $j$  can be expressed as:<sup>[49,50]</sup>

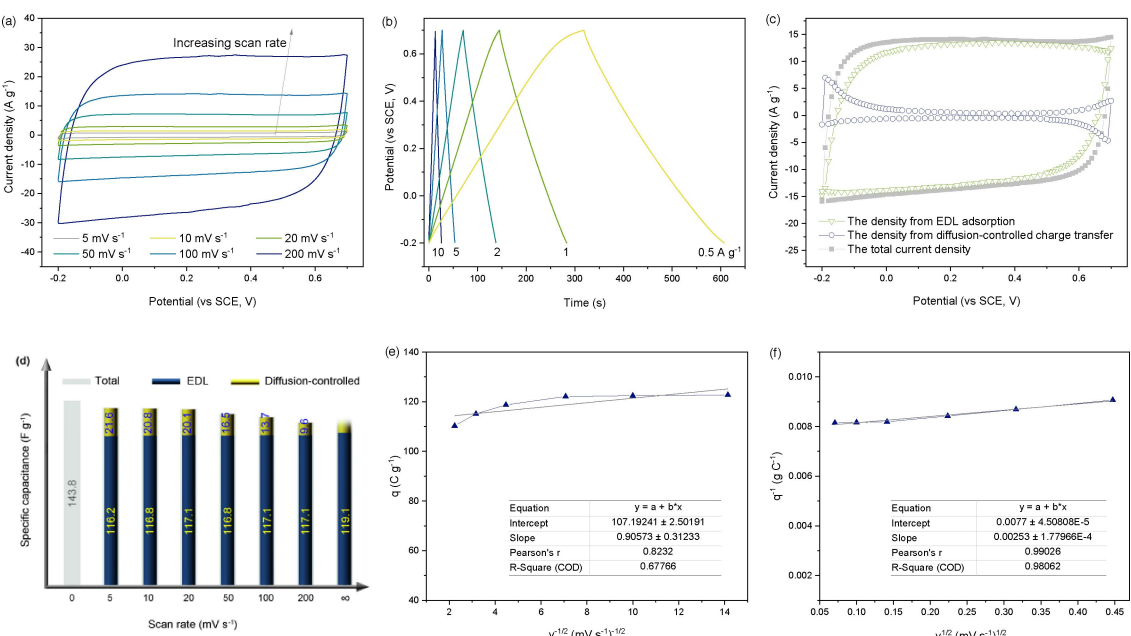


**Figure 4.** The  $\text{NH}_4^+$  storage performance of PEDOT-60: CV curves at various scan rates (a); GCD curves at various charge/discharge current densities (b); The voltammetric response current density (c) and the capacitance (the ones at 0 and  $\infty$  were got by extrapolation) (d) from the different origins when scanned at 100 mV s<sup>-1</sup>; The variations of the surface charge density (e) and total charge density (f) with scan rate.

$$j = k_e v + k_p v^{\frac{1}{2}} \quad (3)$$

where  $k_e$ ,  $k_p$  is the effect factor for surface-controlled process and diffusion-controlled process, respectively;  $v$  is the scan rate ( $\text{Vs}^{-1}$ ). Apparently, the equation can be written as:

$$\frac{j}{v^{\frac{1}{2}}} = k_e v^{\frac{1}{2}} + k_p \quad (4)$$

Equation 4 is a linear expression, so the  $k_e$  and  $k_p$  can be easily obtained from the slope of the line and its intercept on the Y-axis, respectively. By substituting these factors back into equation 3, the contribution from surface-controlled or diffusion-controlled processes can be quantified for a given voltage and scan rate. After a sufficient collection of the  $k_e$  and  $k_p$ , it becomes possible to distinguish between different capacitances. An example is given in Figure 4c, in which the response current density of PEDOT-60 scanned at  $100 \text{ mVs}^{-1}$  is differentiated into the one originating from surface-controlled processes and the one from diffusion-controlled processes. Moreover, their contribution to the total capacitance varies with the scan rate, as shown in Figure 4d. This is because, although  $\text{NH}_4^+$  ions are able to reach the surface of the active material, they do not have enough time to complete the diffusion throughout the active material during a very fast scanning, leading to a reduced share from diffusion-controlled processes. Conversely, at a very slow scan rate, there is enough time for carrier diffusion, so both surface-controlled and diffusion-controlled processes are involved in the charge storage.

Capacitance is the ratio of the amount of electric charge stored between two conductors to a difference in electric potential between them. According to the specific capacitance equation (Equation 1), the amount of charge ( $q$ ) in an electrochemically active material can be expressed as:

$$q = C^* \Delta V = \frac{1}{mv} \int_{V_a}^{V_c} I_v dV = \frac{1}{v} \int_{V_a}^{V_c} j dV \quad (5)$$

When putting Equation 2 into Equation 4, we get:<sup>[51]</sup>

$$q = \int_{V_a}^{V_c} k_e dV + \int_{V_a}^{V_c} k_p v^{-\frac{1}{2}} dV \quad (6)$$

As the  $k_e$  and  $k_p$  are the effect factors for surface-controlled processes and diffusion-controlled processes, respectively, Equation 6 means the total charge ( $q_t$ ) in an electrode comprises the charges adsorbed by the surface-controlled processes ( $q_s$ ) and the ones coming from diffusion-controlled processes. The  $q_s$  can be derived from the  $q$  versus  $v^{-1/2}$  plot by extrapolating  $q$  to  $v=\infty$  (Figure 4e), while  $q_t$  can be got from the  $q^{-1}$  versus  $v^{1/2}$  plot by extrapolating  $q$  to  $v=0$  (Figure 4f).<sup>[52]</sup> These data are summarized in Table 1, revealing that the surface-controlled charge overwhelmingly dominates, constituting over 80% of the total storage.

A lateral comparison further highlights the influence of the ordering of the polymer macromolecules on their electrochemical performance. The charge storage characteristics of the PEDOTs are the same, with almost identical shape of the CV and GCD curves (Figure 5a and 5b, and Figure S5 and S6), but their charge storage capability enhances with the increasing oxidant concentration (Figure 5c). The specific capacitance at a scan rate of  $5 \text{ mVs}^{-1}$ , calculated using Equation 1, is  $73.25$ ,  $86.84$ ,  $98.39$ ,  $113.79$  and  $137.89 \text{ Fg}^{-1}$  for PEDOT-03, PEDOT-07, PEDOT-15, PEDOT-30 and PEDOT-60, respectively (Table 1 also provides the values calculated using Equation 2). In addition, their capacitance retention at high discharge rates (Figure 5d) and cycling stability (Figure 5e) also exhibit an improved trend. At a scan rate of  $200 \text{ mVs}^{-1}$ , PEDOT-60 keeps  $91.92\%$  of the capacitance got at  $5 \text{ mVs}^{-1}$ , compared to  $68.61\%$  for PEDOT-03 (Table 1). After 5000 charge/discharge cycles, PEDOT-60 maintains  $94.08\%$  of its initial capacitance, while it is  $89.73\%$  for PEDOT-03 (Table 1).

Interestingly, the ordering of the macromolecules also affects the charge storage mechanism. Based on the extrapolation of the curves in Figure S7, the total charge and the charge accumulated by surface-controlled processes of a studied sample are obtained (Table 1). The data indicate that the share of  $q_s$  increases with the increasing oxidant concentration, from  $57.48\%$  for PEDOT-03 to  $82.82\%$  for PEDOT-60. This implies that the samples prepared with higher concentration of  $\text{FeCl}_3$  are more inclined to store charge efficiently in the manner of surface adsorption, and vice versa.

**Table 1.** The  $\text{NH}_4^+$  storage performance of the PEDOTs.

Sample	Specific capacitance ( $\text{Fg}^{-1}$ )			Rate capability ( $C_{200}/C_5$ )%	Charge density ( $\text{C g}^{-1}$ )		$(q_s/q_t)$ %	Cycling stability <sup>[d]</sup> %
	$C_{0.5}$ <sup>[a]</sup>	$C_5$ <sup>[b]</sup>	$C_{200}$ <sup>[c]</sup>		$q_s$	$q_t$		
PEDOT-03	105.64	73.25	50.26	68.61	45.31	78.80	57.48	89.73
PEDOT-07	115.47	86.84	68.72	79.13	62.72	81.17	77.25	91.92
PEDOT-15	120.01	98.39	86.52	87.94	77.68	94.93	81.85	93.04
PEDOT-30	140.84	113.79	101.63	89.31	88.74	107.98	82.18	93.86
PEDOT-60	160.41	137.89	126.75	91.92	107.19	129.42	82.82	94.08

<sup>[a]</sup> The specific capacitance obtained at  $0.5 \text{ A g}^{-1}$ ; <sup>[b]</sup> The specific capacitance obtained at  $5 \text{ mVs}^{-1}$ ; <sup>[c]</sup> The specific capacitance obtained at  $200 \text{ mVs}^{-1}$ ; <sup>[d]</sup> The ratio of the initial capacitance to the capacitance of the last cycle.

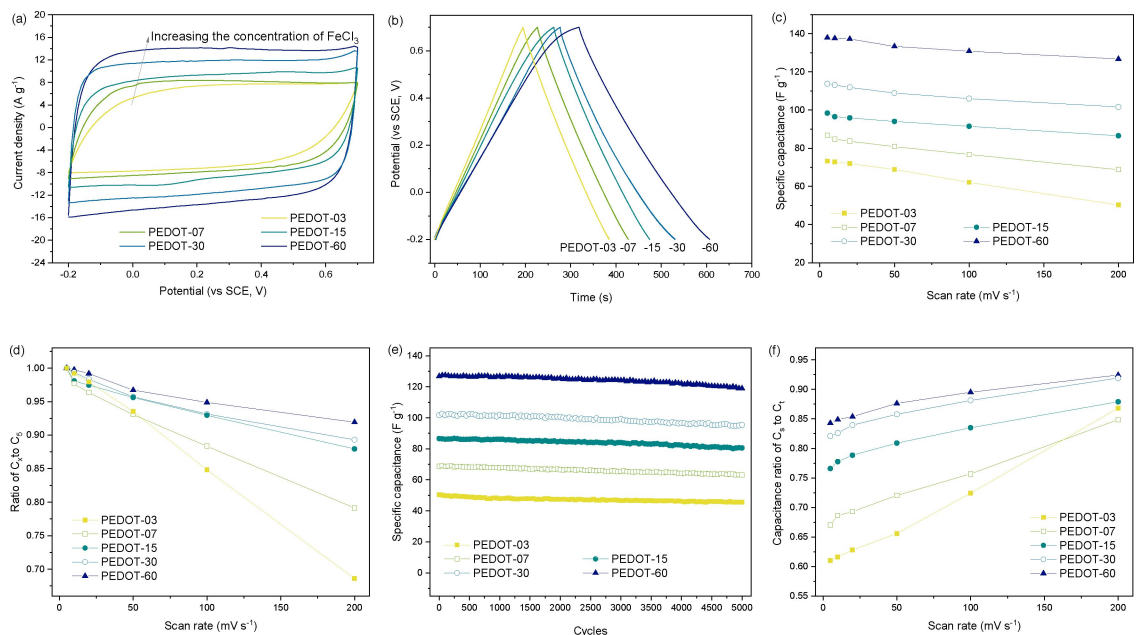


**Figure 5.** The  $\text{NH}_4^+$  storage performance of the PEDOTs: CV curves at  $100 \text{ mV s}^{-1}$  (a); GCD curves at  $0.5 \text{ A g}^{-1}$  (b); The specific capacitances (c) and capacitance retentions ( $C_s$  and  $C_x$  means the specific capacitance at  $5$  and  $x \text{ mV s}^{-1}$ , respectively, d) at various scan rates; Cycling stabilities (e) and The contributions of EDL adsorption at various scan rates (f).

This interpretation is supported by the ratios of surface-controlled capacitance to total capacitance at various scan rates (Figure 5f). The ratio for PEDOT-60 reaches 84.28% of its total capacitance at  $5 \text{ mV s}^{-1}$ , although such a slow rate has been possible to complete the diffusion. In contrast, for PEDOT-03, the increase in diffusion-controlled capacitance causes the surface-controlled capacitance to drop to 61.01% of its total capacitance when the scan rate slows from 200 to  $5 \text{ mV s}^{-1}$ .

### 3. Discussions

#### 3.1. Formation mechanism

The polymerization mechanism of conducting polymers, though not completely understood, is similar.<sup>[53]</sup> Typically, in a chemical polymerization, EDOT monomers are first oxidized to reactive species. These radical cations react with each other to form a dimeric dication, and then the dimeric dications subsequently lose two protons to form dimers and eventually higher oligomers and polymers (Figure 1j).<sup>[54]</sup> Throughout these processes, an oxidant, usually a ferric salt or persulfate, is necessary. Iron oxyhydroxides or oxides can act as a source to supply  $\text{Fe}^{3+}$  ions in weakly acidic aqueous solutions. D'Arcy's group once used HCl vapor to dissolve rust (containing  $\alpha\text{-FeOOH}$ ,  $\gamma\text{-FeOOH}$ , and  $\text{FeSO}_4$  phases) to oxidize EDOT monomers into PEDOT coatings.<sup>[9]</sup> Similarly, the hierarchical oxyhydroxides serve as a continuous supply of the oxidant. Upon the addition of EDOT monomers, the oxidative radical polymerization occurs, in which  $\text{Fe}^{3+}$  ions undergo reduction to  $\text{Fe}^{2+}$ , EDOT monomer is oxidized to EDOT<sup>+</sup> radical cation,

and aquated  $\text{H}^+$  is released. These released  $\text{H}^+$  are able to further lower the pH value around the reaction sites, causing partial dissolution of the iron oxyhydroxides. This, in turn, releases ferric ions until the oxides are completely dissolved. In this manner, the polymerization reaction continues until the solution is depleted of  $\text{Fe}^{3+}$  ions. Figure 1j illustrates a schematic diagram of this process.

We infer two potential pathways for the formation of the PEDOT coatings on these oxyhydroxides. The first one is the  $\text{Fe}^{3+}$  ion supply as described above. The  $\text{Fe}^{3+}$  concentration is quite low in the bulk solution, yet it is relatively high and sustained near the oxides. This localized increase in ion concentration facilitates the polymerization process, resulting in the polymerization readily occurring at or near the surfaces of the oxyhydroxides. This local ion concentration effect is also used for PEDOT electrodeposition.<sup>[5]</sup> The other reason is the favor for low interfacial energy. The radical polymerization of EDOT can proceed anywhere as long as sufficient EDOT<sup>+</sup> cations are available. Consequently, EDOT species, including monomers, incipient oligomers and radical cations, self-assemble into one-dimension clusters due to  $\pi-\pi$  interactions between linear aromatic oligomers, eventually forming cylindrical nanomaterials (Figure S8). This polymerization process, however, is inhibited in our study by the very low concentration of  $\text{Fe}^{3+}$  ions. At such concentrations, the PEDOT nuclei originating from progressive nucleation struggle to sustain growth due to the retarded supply of EDOT<sup>+</sup> cations; on the contrary, the nuclei grown on the oxyhydroxides (instantaneous nucleation) have more opportunities to occur and subsequent development into oligomers because of the lower interfacial energy, and ultimately to mature into the polymer.

### 3.2. Electrochemical kinetic mechanism

The aforementioned analyses, namely, (i) the readiness of PEDOT-60 to store charges via surface-controlled processes, (ii) the consistent contribution of surface-controlled capacitance across various scan rates, and (iii) the fairly small proportion of diffusion-controlled capacitance in the total storages, indicate that the PEDOTs, especially the ones prepared with higher oxidant concentrations, store  $\text{NH}_4^+$  mainly via surface-controlled processes rather than diffusion-controlled ones. This mechanism confers exceptional rate capability to PEDOTs, as evident in Figure 5c and 5d and in Table 1. From a macroscopic perspective, the PEDOT shells are prepared by eliminating the hierarchical iron oxyhydrates, so that both outer and inner surfaces have the opportunity to be in direct contact with the electrolyte, which increases the reactive surfaces. In addition, in applications requiring binders and collectors, such a morphology significantly reduces contact resistances between electrochemically active materials, facilitating efficient charge transfer (Figure 6a). In comparison, binders, which are typically poorly conductive, have to cover the surfaces of conventional nano-

scale PEDOT particles (like those in Figure S8) to bind them together or to bind them with the current collector together. This coverage not only increases the contact resistances but also isolates the particles from the electrolyte, both of which limit the direct exposure of electrochemically active surface (Figure 6b) and resulting in poor charge transfer.

From a microscopic perspective, the FT-TR analysis suggests a gradual amelioration in the degree of polymerization (Figure 2b-d), and the SAXS/WAXS results further quantitatively and intuitively demonstrate the improved crystallinity (Figure 3c-e). Conductive polymers are well-known disordered materials, consisting of polymer chains of different lengths and randomly distributed defects. The mixing of face-on and edge-on orientation deteriorates the pathways for charge transfer.<sup>[55]</sup> The localization of the charge wave functions, caused by the loss of crystal symmetry and long-range order, makes charge transport possible only by quantum mechanical jumps from one localized position to another. Electrons are thus transferred rapidly in the chains, moderately between the chains and slowly between the lamellar stacks.<sup>[56]</sup> In other words, the crystallinity and orderliness of the chains, as well as the relative stacking between

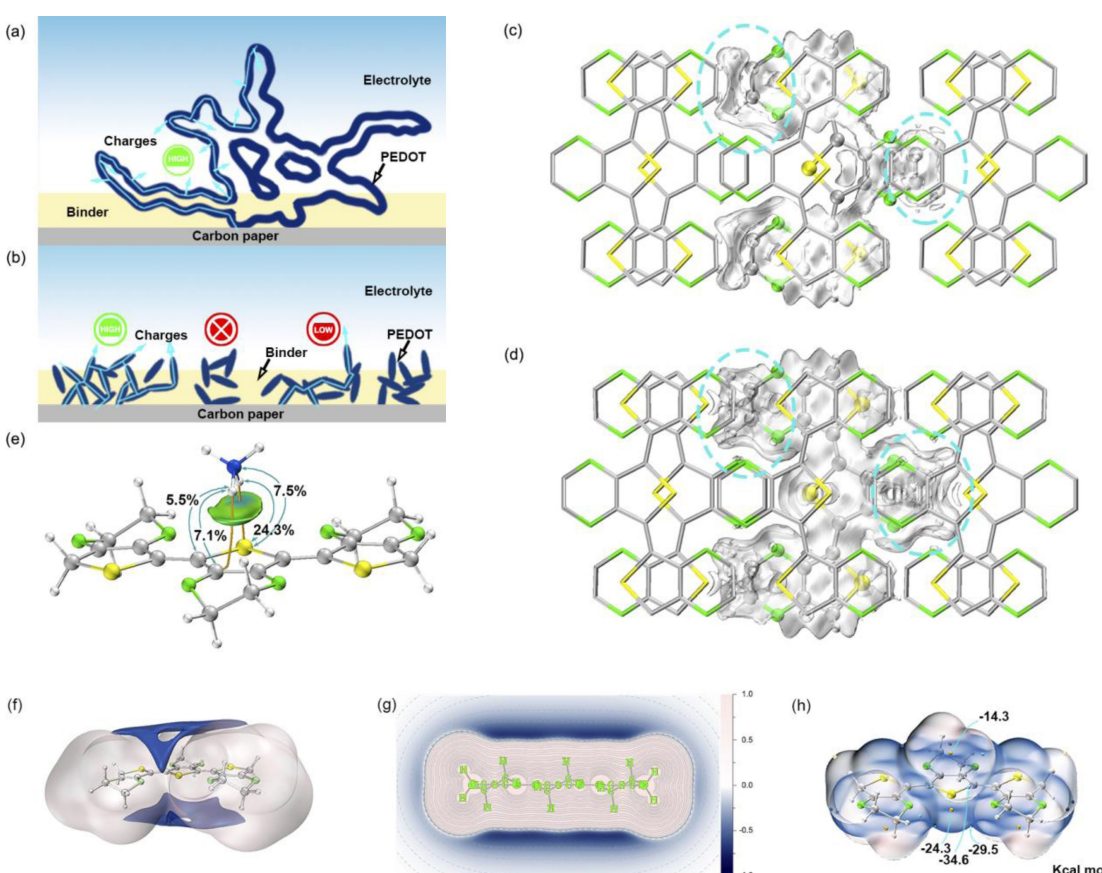


**Figure 6.** Schematic diagram of the conductivity mechanism for the hierarchical PEDOTs (a) and the conventional nanoscale PEDOT particles (b) in an electrode; The inter-chain interactions of PEDOT-03 (c) and PEDOT-60 (d), in which the studied chain is shown in ball-and-stick mode while other chains are shown in stick mode without hydrogen for clarity, and the isovalue is set to 0.015 a.u.; The interactions between PEDOT and  $\text{NH}_4^+$  (e), in which the isovalue of  $\delta g_{\text{inter}}$  is set to 0.008 a.u., and it is colored according to sign ( $\lambda_2$ ) $\rho$  function; The isosurface of PEDOT with Ne as probe atom at a vdw potential of 0.6 Kcal mol<sup>-1</sup> (f), and the corresponding color-filled plane maps with contour lines (g), in which the light red is positive and the dark blue is negative part, respectively. Unit: Kcal mol<sup>-1</sup>; The electrostatic potential on PEDOT (h), in which the light red surface (yellow points) represents the higher (local highest) value, while the blue surface (cyan points) represents the lower (local lowest) value. Unit: Kcal mol<sup>-1</sup>.

the chains determine the transport properties of conjugated conductive polymers.<sup>[55,57]</sup> In this study, the larger grain size increases the proportion of crystalline domains in the macromolecules,<sup>[58]</sup> the shortened lamellar packing reduces the potential barrier for charges hopping from one crystalline domain to others, and the shortened face-to-face distance of the chains results in tighter  $\pi$ -stacking and enhances aggregation, which in turn improves the inter-molecular jump quality of charge carriers.<sup>[59]</sup>

Gharahcheshmeh et. al. once proved that electrical conductivity within a crystallite is highly sensitive to the  $\pi$ - $\pi$  stacking distance and inter-chain charge transfer integral.<sup>[55]</sup> A reduction in the  $\pi$ - $\pi$  stacking distances from 3.50 Å to 3.43 Å results in a remarkable enhancement in conductivity of  $\approx$ 1140%. This is because carrier mobility is proportional to the square of the inter-chain charge transfer integral, while the integral is exponentially related to the  $\pi$ - $\pi$  stacking distance of a conjugated polymer.<sup>[16,57]</sup> Once other factors, such as chain length, crystallite size, and degree of order are determined, inter-chain charge transfer becomes the rate-limiting step.<sup>[15]</sup> To further uncover the interactions between the chains, density functional theory analyses were conducted. The IGMH analysis in Figure 6c and 6d, along with Figure S9, indicates that the shortening of lamellar packing distances or the shortening face-to-face distance of the PFDOT chains strengthens the weak interactions between the packings or chains, and the electron clouds between the chains (paths for electron transfer) overlap (marked with cyan circles in Figure 6c and 6d). These inter-chain coupling leads to progressively intensified delocalization of charge carriers and an extended wave function overlap length.<sup>[60]</sup> Such a concentrated electronic delocalization, coupled with the high planarity of quinoid backbone, mitigates the random diffusion of electrons. Furthermore, the extended wave function may even cover the tie-chains between crystallites, and therefore reducing the random quantum hopping.<sup>[46]</sup> All these factors collectively contribute to enhancing electronic conductivity. Their electrical conductivity is measured to be 583, 801, 932, 1017, 1073 S cm<sup>-1</sup>, respectively.

Notably, the macromolecules exhibit distinct interaction patterns when interacting with non-metallic or metallic cations. In the case of NH<sub>4</sub><sup>+</sup> and Na<sup>+</sup> ions, for example, after geometric optimization, the NH<sub>4</sub><sup>+</sup> ion is located about 3.19 Å above the thiophene ring (Figure 6e and Figure S10a and S10e); while the Na<sup>+</sup> ion appears to be attracted by both the S atom in the thiophene ring and the O atom in the ethylenedioxy ring, eventually settling about 2.70 Å above the macromolecule (Figure S10b and S10f), even though the two ions are placed at the same position away from the macromolecule at the beginning of the optimization. The sign ( $\lambda_2$ ) $\rho$  colored  $\delta g$  <sup>inter</sup> isosurface maps of these interactions are presented in Figure 6e and Figure S10c-f. A thin and broad isosurface appears between the NH<sub>4</sub><sup>+</sup> ion and the thiophene ring, where the green areas signify the prominent weak interactions while the slight blue areas suggest the presence of a strong attraction (more possible in the form of hydrogen bonds). The investigation on van der Waals potential<sup>[61]</sup>

reveals that the most negative region locates above the thiophene rings or between the two face-to-face linear macromolecules. Accordingly, by considering the distance (3.19 Å), NH<sub>4</sub><sup>+</sup> ions uniformly interact with the  $\pi$ - $\pi$  stacking in the PEDOTs via van der Waals interactions (Figure 6f and 6g and Figure S11).<sup>[62]</sup>

Attractive interactions are also observed between the Na<sup>+</sup> ion and the O or S atoms in the PEDOT, although the dispersion-dominated interaction regions are relatively small (Figure S10d and S10f). More than half of the contribution comes from Na-S and Na-O bonds (Figure S12). From the ESP analysis (Figure 6h and Figure S13), it is evident that the macromolecule is covered by an electron cloud, except for the positions closed to the hydrogen atoms, and the positions near the C-S-C and C-O-C groups have more negative potentials (approximately -30 Kcal mol<sup>-1</sup>). Regions with greater negative potentials are known to preferentially attract nucleophiles,<sup>[63]</sup> and therefore, Na<sup>+</sup> ions interact with these sites. Considering the shorter distance (2.70 Å) and the substantial contribution (more than 50%), the interaction is probably dominated by a loose ionic bond (the Na-S bond length in Na<sub>2</sub>S is about 2.44 Å). This interaction is so strong that it is able to disrupt the thiophene backbone planarization (Figure S10f). During charge storage, sodium ions have to diffuse longer distances in the electrolyte and consume more energy to establish/detach the ionic interactions.<sup>[64]</sup> Instead, NH<sub>4</sub><sup>+</sup> ions interact with the macromolecules via weak interactions. This means that firstly the process does not involve ionization energy,<sup>[65]</sup> and secondly the backbone conformation (aromatic/quinone) in the linear chains does not deform and the entropy barrier does not increase. Large entropy has been shown to slow down electrochemical steps.<sup>[66]</sup> In addition, NH<sub>4</sub><sup>+</sup> ions have a smaller molecular weight (18 g mol<sup>-1</sup>) and hydrated ionic size (3.31 Å). The smaller ion size facilitates fast transport in the electrolyte.<sup>[23,67]</sup> Based on these analyses, the no-metallic NH<sub>4</sub><sup>+</sup> ions, as charge carriers, also contribute to the high-rate performance.

## 4. Conclusion

In summary, the PEDOT shells exhibit outstanding performance in capacitive energy storage. When employing non-metallic NH<sub>4</sub><sup>+</sup> ions as charge carriers, PEDOT-60 has a specific capacitance of 137.89 F g<sup>-1</sup> at a scan rate of 5 mVs<sup>-1</sup>, keeps 91.92% of the capacitance at a scan rate of 200 mVs<sup>-1</sup>, and preserves 94.08% of its initial capacitance after 5000 charge/discharge cycles. The concentration of the oxidant, FeCl<sub>3</sub>, significantly influences the morphology, microstructure, and charge storage mechanism of the PEDOT shells. Increasing FeCl<sub>3</sub> concentration induces a gradual transition of the shells from soft to stiff. FT-IR results reveal enhanced polymerization, indicated by the increased absorption ratio of quinoid to ethylenedioxy (from 0.57 to 0.82) and decreased integration ratio of the characteristic C-S-C bond in the thiophene ring (from 0.88 to 0.76). The quantitative analysis of SAXS/WAXS confirms improved crystallinity, evidenced by the

shorter lamellar packing distance between macromolecular chains (from 7.85 to 6.95 Å) and the closer face-to-face distance of the chains (from 3.47 to 3.44 Å), as well as an expanded grain size, from 33.64 to 59.23 Å along the (020) plane and from 81.10 to 186.91 Å along the (100) plane. The enhanced polymerization and crystallinity strengthen weak interactions between the chain and the packings, intensify delocalization of charge carriers, and extend the wave function overlap length. Combined with van der Waals interactions between  $\text{NH}_4^+$  ions and  $\pi-\pi$  stacking, these factors contribute to efficient surface-controlled processes during  $\text{NH}_4^+$  ion storage in the PEDOT shells.

## Supporting Information

Supporting Information is available from the Wiley Online Library or from the author.

## Acknowledgements

The authors are grateful for financial support from the General scientific research projects of Zhejiang Provincial Department of Education (No. Y202352865) and the Zhejiang Provincial Natural Science Foundation of China (Nos. LZ22B060001).

## Conflict of Interest

The authors declare no conflict of interest.

**Keywords:** Poly(3,4-ethylenedioxythiophene) • Non-metallic cations •  $\text{NH}_4^+$  storage • Hierarchical structure • Capacitive energy storage

- [1] Y. W. Park, A. J. Heeger, M. A. Drury, A. G. Macdiarmid, *J. Chem. Phys.* **1980**, *73*, 946.
- [2] T. G. Yun, X. Chen, J. Y. Cheong, *Batteries & Supercaps* **2022**, *6*, e202200454.
- [3] L. V. Kayser, D. J. Lipomi, *Adv. Mater.* **2019**, *31*, 1806133.
- [4] B. Xiao, J. Li, H. Xu, J. Huang, Y. Luo, K. Xiao, Z. Liu, *Angew. Chem. Int. Ed.* **2023**, *62*, e202309614.
- [5] V. R. Feig, H. Tran, M. Lee, K. Liu, Z. Huang, L. Beker, D. G. Mackanic, Z. Bao, *Adv. Mater.* **2019**, *31*, 1902869.
- [6] X. Wang, X. Zhang, L. Sun, D. Lee, S. Lee, M. Wang, J. Zhao, Y. Shao-Horn, M. Dincă, T. Palacios, K. K. Gleason, *Sci. Adv.* **2018**, *4*, 5780.
- [7] Q. Zhao, R. Jamal, L. Zhang, M. Wang, T. Abdiriyim, *Nanoscale Res. Lett.* **2014**, *9*, 557.
- [8] M. V. Fabretto, D. R. Evans, M. Mueller, K. Zuber, P. Hojati-Talemi, R. D. Short, G. G. Wallace, P. J. Murphy, *Chem. Mater.* **2012**, *24*, 3998.
- [9] Y. Diao, H. Chen, Y. Lu, L. M. Santino, H. Wang, J. M. D. Arcy, *ACS Appl. Energ. Mater.* **2019**, *2*, 3435.
- [10] Y. Cai, R. Wang, L. Xu, F. Jiang, A. Liang, X. Duan, J. Xu, W. Zhou, Q. Xu, X. Lu, *J. Electrochem. Soc.* **2020**, *167*, 80538.
- [11] K. Zhang, J. Qiu, S. Wang, *Nanoscale* **2016**, *8*, 8033.
- [12] M. Rajesh, C. J. Raj, R. Manikandan, B. C. Kim, S. Y. Park, K. H. Yu, *Mater. Today Energy* **2017**, *6*, 96.
- [13] I. Ivanko, J. Pánek, J. Svoboda, A. Zhigunov, E. Tomšík, *J. Mater. Chem. C* **2019**, *7*, 7013.
- [14] B. Cho, K. S. Park, J. Baek, H. S. Oh, Y. K. Lee, M. M. Sung, *Nano Lett.* **2014**, *14*, 3321.
- [15] M. H. Gharahcheshmeh, K. K. Gleason, *Mater. Today* **2020**, *8*, 100086.
- [16] K. K. Gleason, *Nat. Rev. Phys.* **2020**, *2*, 347.
- [17] G. Liang, F. Mo, X. Ji, C. Zhi, *Nature Rev. Mater.* **2020**, *6*, 109.
- [18] H. Jiang, J. J. Hong, X. Wu, T. W. Surta, Y. Qi, S. Dong, Z. Li, D. P. Leonard, J. J. Holoubek, J. C. Wong, J. J. Razink, X. Zhang, X. Ji, *J. Am. Chem. Soc.* **2018**, *140*, 11556.
- [19] R. Zheng, Y. Li, H. Yu, X. Zhang, D. Yang, L. Yan, Y. Li, J. Shu, B. Su, *Angew. Chem. Int. Ed.* **2023**, *62*, e202301629.
- [20] H. Yu, J. Xu, C. Deng, M. Xia, X. Zhang, J. Shu, Z. Wang, *ACS Appl. Energ. Mater.* **2021**, *4*, 9594.
- [21] S. Dong, W. Shin, H. Jiang, X. Wu, Z. Li, J. Holoubek, W. F. Stickle, B. Key, C. Liu, J. Lu, P. A. Greaney, X. Zhang, X. Ji, *Chem* **2019**, *5*, 1537.
- [22] L. Yang, W. Zheng, J. Halim, J. Rosen, Z. Sun, M. W. Barsoum, *Batteries & Supercaps* **6**, e202200432.
- [23] X. Wu, J. J. Hong, W. Shin, L. Ma, T. Liu, X. Bi, Y. Yuan, Y. Qi, T. W. Surta, W. Huang, J. Neuefeind, T. Wu, P. A. Greaney, J. Lu, X. Ji, *Nat. Energy* **2019**, *4*, 123.
- [24] G. Liang, Y. Wang, Z. Huang, F. Mo, X. Li, Q. Yang, D. Wang, H. Li, S. Chen, C. Zhi, *Adv. Mater.* **2020**, *32*, 1907802.
- [25] Z. Tian, V. S. Kale, Y. Wang, S. Kandambeth, J. Czaban-Józwiak, O. Shekhah, M. Eddaaoud, H. N. Alshareef, *J. Am. Chem. Soc.* **2021**, *143*, 19178.
- [26] Q. Chen, J. Jin, M. Song, X. Zhang, H. Li, J. Zhang, G. Hou, Y. Tang, L. Mai, L. Zhou, *Adv. Mater.* **2022**, *34*, 2107992.
- [27] N. M. Chola, R. K. Nagarale, *Batteries & Supercaps* **2022**, *5*, e202200221.
- [28] B. Xiao, W. J. Cai, P. Y. Wu, K. Xiao, Z. Liu, *Renewables* **2023**, *1*, 227.
- [29] M. N. Gueye, A. Carella, N. Massonnet, E. Yvenou, S. Brenet, J. Faure-Vincent, S. Pouget, F. Rieutord, H. Okuno, A. Benayad, R. Demadrille, J. Simonato, *Chem. Mater.* **2016**, *28*, 3462.
- [30] B. Xiao, R. Lin, K. Xiao, Z. Liu, *J. Power Sources* **2022**, *530*, 231307.
- [31] X. X. Li, X. H. Deng, Q. J. Li, S. Huang, K. Xiao, Z. Liu, *Electrochim. Acta* **2018**, *264*, 46.
- [32] T. Lu, Q. Chen, *J. Comput. Chem.* **2022**, *43*, 539.
- [33] T. Lu, F. Chen, *J. Comput. Chem.* **2012**, *33*, 580.
- [34] W. Humphrey, A. Dalke, K. Schulten, *J. Mol. Graphics* **1996**, *14*, 33.
- [35] F. Neese, *Wiley Interdiscip. Rev.: Comput. Mol. Sci.* **2012**, *2*, 73.
- [36] T. D. Kühne, M. Iannuzzi, M. D. Ben, V. V. Rybkin, P. Seewald, F. Stein, T. Laino, R. Z. Khalilu, O. Schütt, F. Schiffmann, D. Golze, J. Wilhelm, S. Chulkov, M. H. Bani-Hashemian, V. Weber, U. Borštník, M. Taillefumier, A. S. Jakobovits, A. Lazzaro, H. Pabst, T. Müller, R. Schade, M. Guidon, S. Andermatt, N. Holmberg, G. K. Schenter, A. Hehn, A. Bussy, F. Belleflamme, G. Tabacchi, A. Glöß, M. Lass, I. Bethune, C. J. Mundy, C. Plessl, M. Watkins, J. Vandevondrele, M. Krack, J. Hutter, *J. Chem. Phys.* **2020**, *152*, 194103.
- [37] M. Mirabedini, H. Vergnes, N. Caussé, C. Vahlas, B. Caussat, *Synth. Met.* **2020**, *266*, 116419.
- [38] S. Musić, S. Krehula, S. Popović, *Mater. Lett.* **2004**, *58*, 2640.
- [39] D. Maiti, P. Sujatha Devi, *Mater. Chem. Phys.* **2015**, *154*, 144.
- [40] D. Ni, Y. Chen, H. Song, C. Liu, X. Yang, K. Cai, *J. Mater. Chem. A* **2019**, *7*, 1323.
- [41] S. G. Im, K. K. Gleason, *Macromolecules* **2007**, *40*, 6552.
- [42] N. Massonnet, A. Carella, A. de Geyer, J. Faure-Vincent, J. Simonato, *Chem. Sci.* **2015**, *6*, 412.
- [43] D. Ni, H. Song, Y. Chen, K. Cai, *Energy* **2019**, *170*, 53.
- [44] P. Simon, Y. Gogotsi, B. Dunn, *Science* **2014**, *343*, 1210.
- [45] Z. Yang, J. Ma, B. Bai, A. Qiu, D. Losic, D. Shi, M. Chen, *Electrochim. Acta* **2019**, *322*, 134769.
- [46] K. D. Fong, T. Wang, H. Kim, R. V. Kumar, S. K. Smoukov, *ACS Energy Lett.* **2017**, *2*, 2014.
- [47] A. Mocaér, F. Pillier, A. Pailleret, *Electrochim. Acta* **2021**, *389*, 138651.
- [48] A. V. Volkov, K. Wijeratne, E. Mitraka, U. Ail, D. Zhao, K. Tybrandt, J. W. Andreassen, M. Berggren, X. Crispin, I. V. Zozoulenko, *Adv. Funct. Mater.* **2017**, *27*, 1700329.
- [49] X. Meng, L. Lu, C. Sun, *ACS Appl. Mater. Interfaces* **2018**, *10*, 16474.
- [50] Z. Li, S. Gadipelli, H. Li, C. A. Howard, D. J. L. Brett, P. R. Shearing, Z. Guo, I. P. Parkin, F. Li, *Nat. Energy* **2020**, *5*, 160.
- [51] P. Soudan, J. Gaudet, D. Guay, D. Bélanger, R. Schulz, *Chem. Mater.* **2002**, *14*, 1210.
- [52] S. Ardizzone, G. Fregonara, S. Trasatti, *Electrochim. Acta* **1990**, *35*, 263.
- [53] S. Sadki, P. Schottland, N. Brodie, G. Sabouraud, *Chem. Soc. Rev.* **2000**, *29*, 283.
- [54] M. Mueller, M. Fabretto, D. Evans, P. Hojati-Talemi, C. Gruber, P. Murphy, *Polymer* **2012**, *53*, 2146.

- [55] M. Heydari Gharahcheshmeh, M. T. Robinson, E. F. Gleason, K. K. Gleason, *Adv. Funct. Mater.* **2020**, *31*, 2008712.
- [56] Y. Yao, H. Dong, W. Hu, *Adv. Mater.* **2015**, *28*, 4513.
- [57] V. Coropceanu, J. Cornil, D. A. Da Silva Filho, Y. Olivier, R. Silbey, J. L. Brédas, *Chem. Rev.* **2007**, 926.
- [58] A. C. Hinckley, S. C. Andrews, M. T. Dunham, A. Sood, M. T. Barako, S. Au Schneider, M. F. Toney, K. E. Goodson, Z. Bao, *Adv. Electron. Mater.* **2021**, *7*, 2001190.
- [59] J. Rivnay, S. Inal, B. A. Collins, M. Sessolo, E. Stavrinidou, X. Strakosas, C. Tassone, D. M. Delongchamp, G. G. Malliaras, *Nat. Commun.* **2016**, *7*, 10.
- [60] I. Zozoulenko, A. Singh, S. K. Singh, V. Gueskine, X. Crispin, M. Berggren, *ACS Appl. Polym. Mater.* **2019**, *1*, 83.
- [61] T. Lu, Q. Chen, *J. Mol. Model.* **2020**, *26*, 10.
- [62] T. Lu, Z. Liu, Q. Chen, *Mater. Sci. Eng. B* **2021**, *273*, 115425.
- [63] J. S. Murray, P. Politzer, *Encyclopedia Computat. Chem.* **2002**, *2*, 912.
- [64] C. Liu, Z. G. Neale, G. Cao, *Mater. Today* **2016**, *19*, 109.
- [65] C. Choi, D. S. Ashby, D. M. Butts, R. H. Deblock, Q. Wei, J. Lau, B. Dunn, *Nat. Rev. Mater.* **2020**, *5*, 5.
- [66] G. Rebetez, O. Bardagot, J. Affolter, J. Réhault, N. Banerji, *Adv. Funct. Mater.* **2022**, *32*, 2105821.
- [67] S. F. Kuchena, Y. Wang, *ACS Appl. Energ. Mater.* **2020**, *3*, 11690.

Manuscript received: November 6, 2023

Revised manuscript received: December 26, 2023

Accepted manuscript online: January 14, 2024

Version of record online: January 31, 2024